










High-Q cavity interface for color centers in thin film diamond

Received: 6 February 2024

Accepted: 17 July 2024

Published online: 28 July 2024

 Check for updates

Sophie W. Ding ¹✉, Michael Haas¹, Xinghan Guo ², Kazuhiro Kuruma^{1,3}, Chang Jin ¹, Zixi Li ², David D. Awschalom ^{2,4}, Nazar Deegan ^{2,4}, F. Joseph Heremans ^{2,4}, Alexander A. High ^{2,4}✉ & Marko Loncar ¹✉

Quantum information technology offers the potential to realize unprecedented computational resources via secure channels distributing entanglement between quantum computers. Diamond, as a host to optically-accessible spin qubits, is a leading platform to realize quantum memory nodes needed to extend such quantum links. Photonic crystal (PhC) cavities enhance light-matter interaction and are essential for an efficient interface between spins and photons that are used to store and communicate quantum information respectively. Here, we demonstrate one- and two-dimensional PhC cavities fabricated in thin-film diamonds, featuring quality factors (Q) of 1.8×10^5 and 1.6×10^5 , respectively, the highest Qs for visible PhC cavities realized in any material. Importantly, our fabrication process is simple and high-yield, based on conventional planar fabrication techniques, in contrast to the previous with complex undercut processes. We also demonstrate fiber-coupled 1D PhC cavities with high photon extraction efficiency, and optical coupling between a single SiV center and such a cavity at 4 K achieving a Purcell factor of 18. The demonstrated photonic platform may fundamentally improve the performance and scalability of quantum nodes and expedite the development of related technologies.

Diamond, as a host to atom-like defects with optically accessible long-lived spin qubits, has emerged as a compelling platform for applications in quantum sensing^{1–4} and communication^{5–8}. Among diamond color centers, nitrogen vacancies (NV)^{1–5}, silicon vacancies (SiV)^{6,7,9–11}, and tin vacancies (SnV)^{8,12–14} are particularly promising and have enabled many state-of-the-art demonstrations of quantum communication. Fundamentally, practical quantum communication requires fast and low-loss transfer of quantum information between spins (stationary qubits/quantum memory) and photons (flying qubits), which translates to figures of merit like bandwidth and fidelity. Therefore, achieving efficient spin-photon interfaces is crucial for a wide range of applications. In diamonds,

these interfaces have been realized by embedding the emitters within optical structures, including microcavities¹⁵, micro rings/microdisks¹⁶, waveguides^{8,11,17}, and nanophotonic cavities^{6,9,12,13,18,19}, which have been enabled by steady progress in diamond fabrication techniques. Among all structures, photonic crystal (PhC) cavities are one of the most efficient spin-photon interfaces because they support optical modes with high-quality factors (Q) and small mode volumes (V), which greatly enhances light-matter interactions and allow for efficient control and readout of the emitter spin state. As a result, PhC cavities have been utilized in a diverse range of qubit platforms, including quantum dots²⁰, defects in Si or SiC^{21–23}, and rare-earth ions in host materials^{24–26}.

¹John A. Paulson School of Engineering and Applied Sciences, Harvard University, Cambridge, Massachusetts, USA. ²Pritzker School of Molecular Engineering, University of Chicago, Chicago, IL, USA. ³Research Center for Advanced Science and Technology, The University of Tokyo, Meguro-ku, Tokyo, Japan. ⁴Center for Molecular Engineering and Materials Science Division, Argonne National Laboratory, Lemont, IL, USA. ✉e-mail: wding@g.harvard.edu; ahigh@uchicago.edu; loncar@g.harvard.edu

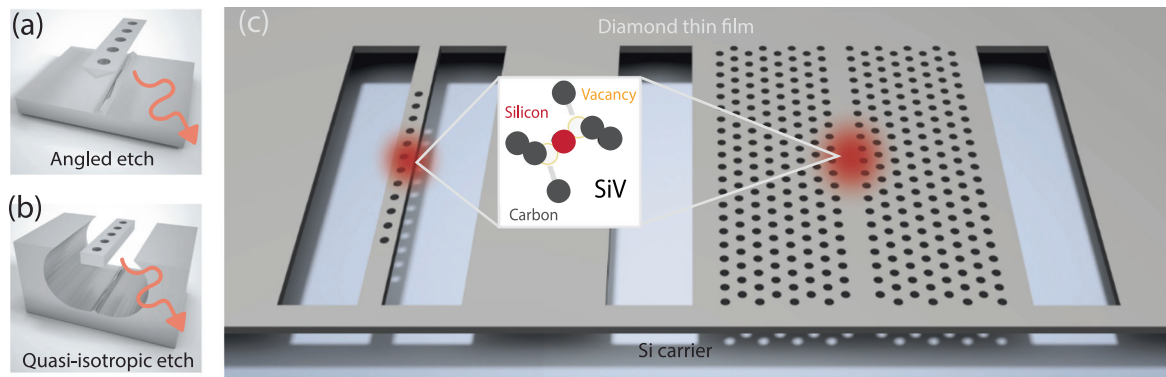


Fig. 1 | State-of-art high-Q suspended PhC cavities fabrication methods.

a Angled etch of a 1D PhC cavity. The structure has a characteristic triangular cross-section due to the nature of the fabrication process. Due to the shallow angle of the ion beam, which would graze the top edge of nearby structures, dense patterns are prohibited. **b** Quasi-isotropic etch of a 1D PhC cavity. The suspension is achieved by an isotropic O_2 reactive-ion etch process. The disadvantage of this method is the long undercutting time that scales with beam width. In both (a) and

(b), the structure is carved out of a bulk diamond and usually has visible artifacts/roughness on the bottom of the nanobeam due to the undercutting. **c** This work: thin film fabrication of 1D and 2D PhC cavities. This approach relies on top-down etching and undercutting of the handle substrate, so it simplifies the fabrication and avoids the roughness of the bottom surface. As a result, this approach leads to exceedingly higher Qs and also allows for more versatile photonic circuits to be realized.

Table 1 | Visible and telecom wavelength suspended diamond PhCs and visible wavelength suspended PhCs in other low-loss visible photonic materials

Cavity type, material	Wavelength (nm)	Q	V (λ/n) ³	Method	Reference
1D, diamond	737	$8.3 \times 10^4 / 1.8 \times 10^5$	0.5	Thin film	This work
1D, diamond	637	1.4×10^4	~1	Quasi-isotropic etching	Mouradian ¹⁸
1D, diamond	737	2.0×10^4	0.5	Angle etching	Bhaskar ⁵
1D, diamond	660	2.4×10^4	0.5	Photoelectrochemical etching	Lee ³¹
1D, diamond	1529 (telecom)	$1.8 \times 10^5 / 2.7 \times 10^5$	0.57	Angle etching	Burek ⁴²
1D, SiN	780	1.1×10^5	0.4	Thin film	Samutpraphoot ⁴⁵
1D, AlN	403	6.9×10^3	1.6	Thin film	Sergent ⁴⁶
1D, 4H-SiC	700	7×10^3	0.5	Photoelectrochemical etching	Bracher ⁴⁷
1D, GaP	744	3.0×10^4	~1	Monolithic	Chakravarthi ⁴⁸
1D, InGaP	841	2.1×10^4	0.64	Monolithic	Saber ⁴⁹
2D, diamond	746	1.6×10^5	2.18	Thin film	This work
2D, diamond	645	8×10^3	0.35	Fib	Jung ¹⁹
2D, diamond	1470 (telecom)	1.8×10^3	2.15	Thin film	Kuruma ²⁹

Several methods have been developed to fabricate diamond nanophotonic structures from bulk diamond substrates, including the focused-ion-beam (FIB) milling¹⁹, Faraday-cage angled etching²⁷, and approaches based on reactive-ion-beam (RIE) angled etching^{6,9} (Fig. 1a) or quasi-isotropic etching^{12,13,18} (Fig. 1b). Both angled and quasi-isotropic etching are the state-of-the-art methods and most popular as a result. However, despite great efforts, these methods typically result in visible PhC cavities with Q factors up to the low $\sim 10^4$ range, much lower than the simulated values $> 10^6$, likely limited by fabrication imperfections such as roughness of etched surfaces induced by complex undercutting processes²⁸. In parallel, diamond thin films generated by substrate thinning and ion-slicing followed by regrowth are explored as the tried-and-true method, due to their potential to simplify and improve fabrication by eliminating undercutting. However, the PhC cavity Qs fabricated using these approaches have been limited to $\sim 10^3$, due to thickness variation and imperfect diamond crystal quality²⁹⁻³¹. They are usually incompatible with quantum networking demonstrations for practical reasons, so the bulk machining methods are still the workhorse in the quantum diamond photonics community today. Therefore, a new thin-film platform and fabrication pathway that improves fabrication capability and maintains high diamond quality are needed to enhance the performance of photonic components in diamond.

In this paper, we demonstrate a thin film diamond photonic platform and realize optical cavities in the visible wavelength range featuring record-high Q factors coupled to stable SiV centers. In our approach, we use a high-quality and homogenous thin film diamond bonded to a silicon oxide/silicon handle wafer. The film is created through ion implantation in bulk diamond, regrowth, electrochemical etching, and transfer printing³². We design and fabricate 1D and 2D PhC diamond cavities operating at 737 nm wavelength range and measure a Q-factor up to 1.8×10^5 , a record for visible PhC cavities fabricated in any material (Table 1). We also fabricate 1D PhCs critically coupled to a feeding waveguide and measure loaded Q of 8.4×10^4 (intrinsic Q $\sim 1.8 \times 10^5$) and a waveguide-cavity coupling efficiency of $\sim 65\%$. We show that this fabrication method exhibits high yield and uniformity: 93% (53 out of 57) of the cavities feature high-Q modes with resonances matched closely to the designed resonances. Finally, we demonstrate the coupling of implanted SiVs to fabricated diamond cavities and observe the three-fold reduction of their radiative lifetime, achieving a Purcell factor of 13. We expect the exceptional cavity performance, high-yield fabrication process, and excellent SiV properties of this new platform to further advance the field of quantum photonics as efficient spin-photon interfaces for color centers in diamond and beyond.

Result

Device fabrication

In our approach, we begin by generating diamond thin films by ion slicing and overgrowth and then use a transfer printing process to directly bond the thin films to a SiO₂/Si substrate³². The size and thickness of the diamond film are $\sim 200 \times 200$ nm and 160 nm, respectively. The film has a surface roughness < 0.3 nm and thickness variation ~ 1 nm, both essential for minimizing optical scattering losses and achieving uniform, high-Q cavities. The SiVs are generated through implantation across the membrane before the transfer, resulting in randomly distributed SiVs. This thin-film diamond has been previously shown to host emitters with promising optical and spin properties³², satisfying one of the prerequisites of a promising platform for spin-photon interface. The fabrication process used to realize PhCs in diamond thin films is summarized in Fig. 2a. Scanning electron microscope (SEM) images of fabricated 1D and 2D PhC

cavities are shown in Fig. 2b, c. The 1D cavities (lattice constant $a_{1D} = 184 - 226$ nm and hole radius $r_{1d} = 65$ nm) are formed by introducing a quadratic hole shift near the waveguide center¹², while the 2D cavities ($a_{2D} = 236 - 269$ nm and $r_{2d} = 65$ nm) are formed by shifting the center holes outwards in the PhC line-defect waveguide²⁹. The details of 1D and 2D cavity designs and resulting field profiles can be found in Methods. The typical simulated Q and V for our 1D (2D) cavities are $\sim 1.0 \times 10^6$ ($\sim 7.6 \times 10^5$) and ~ 0.5 (~ 2.9) $(\lambda/n)^3$.

For practical applications, it is important to interface the cavity with a waveguide and, eventually, a fiber to efficiently transfer quantum information between local spins and propagating photons. Therefore, we also fabricate 1D PhC coupled to a feeding waveguide Fig. 2e by reducing the number of holes in the photonic crystal mirror on one side of the waveguide (see “Methods”). This results in the light preferentially coupling out of the cavity from the feeding waveguide and leading to a simulated cavity Q of 1.9×10^5 (for $a = 255$ nm). The

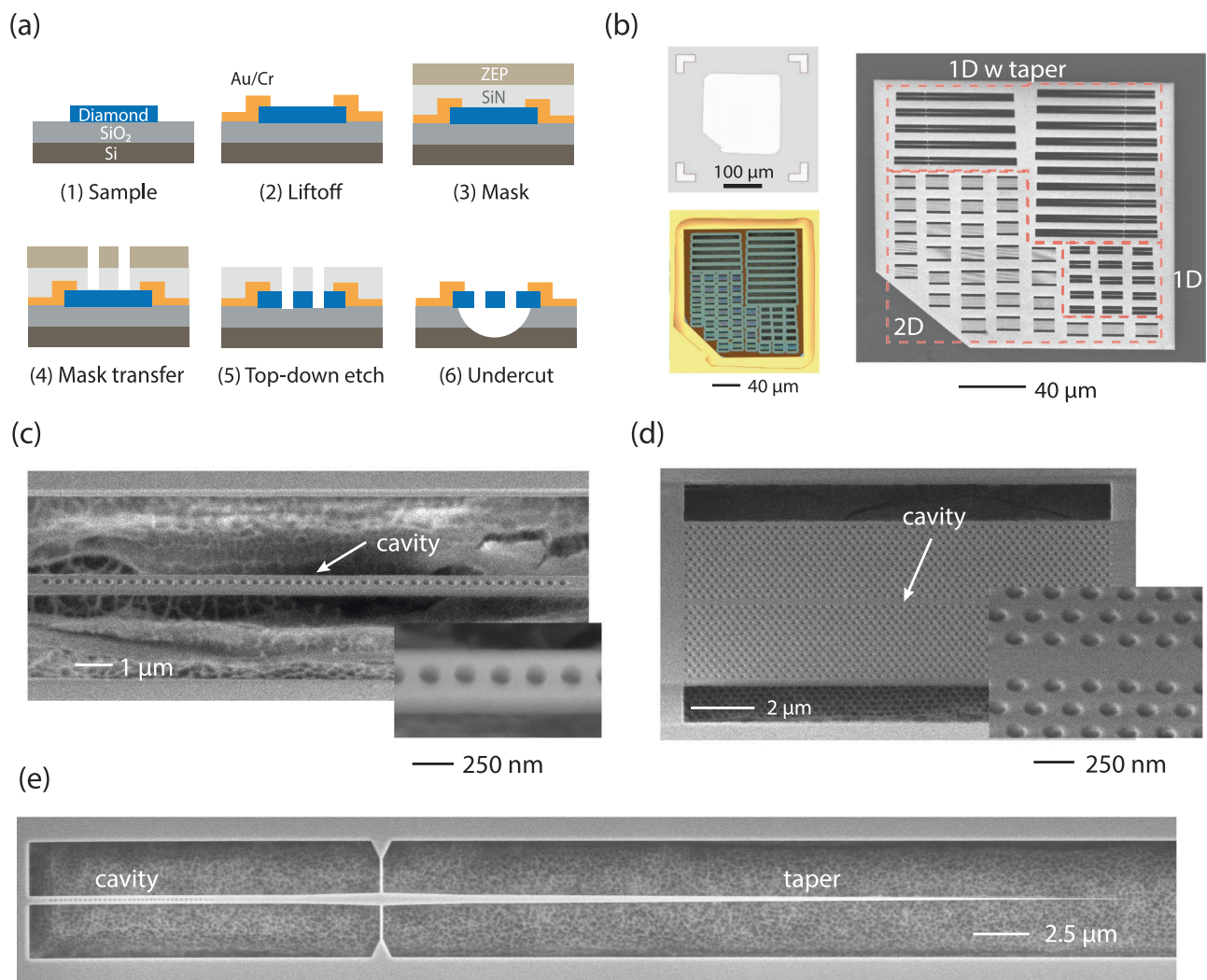


Fig. 2 | Fabrication of high-Q PhC cavities on a thin-film diamond membrane.

a Fabrication flow of the devices based on a thin-film diamond platform.: (1) The diamond with implanted SiV is bonded to the SiO₂/Si substrate; (2) A liftoff of Cr/Au metal stack is performed to define a “frame” around the film in order to secure it on the carrier chip and to prevent delamination; (3) a silicon nitride (SiN) hard mask is deposited using plasma-enhanced chemical vapor deposition (PECVD) with electron beam (EB) resist ZEP520A on top; (4) The cavity pattern is written using EB lithography, and is transferred onto the SiN hard mask using plasma reactive ion etching (RIE) in SF₆ and H₂ chemistry; (5) After removing the EB resist, the pattern is etched into diamond using RIE in O₂ chemistry; (6) Finally, hydrofluoric acid (HF) is used to remove the SiN mask and the 1-μm oxide sacrificial layer underneath. To

introduce additional separation between the diamond film and underlying substrate, the handle wafer is exposed to XeF₂ to etch a deep trench ($> 1 \mu\text{m}$) under the membrane to avoid optical losses via coupling between the diamond membrane and silicon substrate. **b** Left top and bottom panels are microscope images of the sample before and after fabrication. The right panel is the SEM image of the fabricated sample. **c** The SEM image of the 1D PhC cavity. The inset shows the details of the holes. Both are taken at a 45-degree angle. **d** The SEM image of the 2D PhC cavity. The inset shows the details of the holes. Both are taken at a 45-degree angle. **e** The SEM image of the 1D PhC cavity with the taper. The geometry is formed by removing 9 holes on one side from the symmetric 1D cavity design to allow for more preferential coupling to the tapered waveguide side of the structure.

waveguide is tapered at the end (< 60 nm tip width) to allow efficient coupling to a tapered fiber^{33,34}.

Device characterization: 1D and 2D photonic crystal

The fabricated devices are first characterized by photoluminescence (PL) measurements at room temperature (see “Method”). Figure 3a, b show the PL spectra measured for 1D and 2D PhC cavities with different lattice constants, $a_{1D/2D}$. The broad peak at 737 nm is the emission of SiV centers. For 1D PhC cavities, we observe sharp peaks corresponding to the fundamental and high-order (2nd and 3rd) modes. A clear red-shift of their resonant wavelengths is observed as the values of a increase. The measured wavelengths of fundamental modes are in good agreement with the simulations (see the upper panel of Fig. 3c). 2D PhC cavities also exhibit peaks corresponding to the band edges and fundamental modes, and show a shift of the cavity wavelengths as a becomes larger, which is consistent with the simulation as well (see the lower panel of Fig. 3c).

This fabrication method exhibits high uniformity (resonances close to simulation) and high yield (high-Q modes) for both 1D and 2D PhC cavities: from Fig. 3c, we estimate the standard deviation of the measured wavelengths from the simulation to be 1.0% and 1.1% (7.6 nm and 8.2 nm) for 1D and 2D cavities, respectively. Typically, the tuning range is -10 nm with nitrogen gas deposition at 4 K or 100 mK environments without sacrificing device performances, so these devices are well within the tuning range. We fit the cavity spectra observed in Fig. 3a, b and find that 100% (30 out of 30) of all 1D cavities and 85% (23 out of 27) of all 2D cavities characterized feature spectrometer-limited quality factors of $Q > -2 \times 10^4$.

To further resolve the high-Q cavity resonances, we perform cross-polarized measurements using a tunable CW laser²⁹, as schematically shown in Fig. 4a. We scan the laser across the cavity resonance and detect the scattered light from the sample by an

avalanche photodiode (APD). Figure 4c, d shows the reflection spectra of the fundamental cavity modes measured for 1D and 2D cavities with the highest Q factors. The peaks are fitted to a Lorentzian function, and the Q factors obtained are 1.83×10^5 and 1.60×10^5 , respectively. We note that the Q value for a 1D PhC device is one order of magnitude higher than those previously reported in visible diamond PhC cavities, setting a record for visible PhC cavities fabricated in any material (Table 1). Furthermore, our method is compatible with the fabrication of state-of-the-art 2D PhC cavities in diamond that are difficult to make using bulk machining approaches or previous thin film diamond approaches: we demonstrate 2D PhC devices with Q factors that are 20 - 100 times higher than those shown before (Table 1). Lastly, most measured 1D and 2D cavities on the same membrane exhibit Q factors over 0.5×10^5 , as shown in Fig. 4f, which further showcases the uniformity and yield of this platform.

Furthermore, our method is compatible with the fabrication of state-of-the-art 2D PhC cavities in diamond that are difficult to make using bulk machining approaches or previous thin film diamond approaches: The highest Q factor achieved in the 2D PhC device also demonstrates 2D PhC devices with Q factors that are 20 - 100 times higher than previous values reported using quasi-isotropic etching and thin film based approach those shown before (Table 1), suggesting the usefulness of our platform for the realization of high experimental Q factors. Lastly, most measured 1D and 2D cavities on the same membrane exhibit Q factors over 5×10^4 , as shown in Fig. 4f, which further showcases the uniformity and yield of this platform.

To characterize the 1D PhC cavities coupled to a waveguide, we use an optical fiber coupling system, as shown in Fig. 4b. The light from the tunable laser is sent to the tapered waveguide through the optical fiber, and the reflected light is detected by an APD. We use a low laser power of -pW to avoid distortion of the cavity spectrum due to the

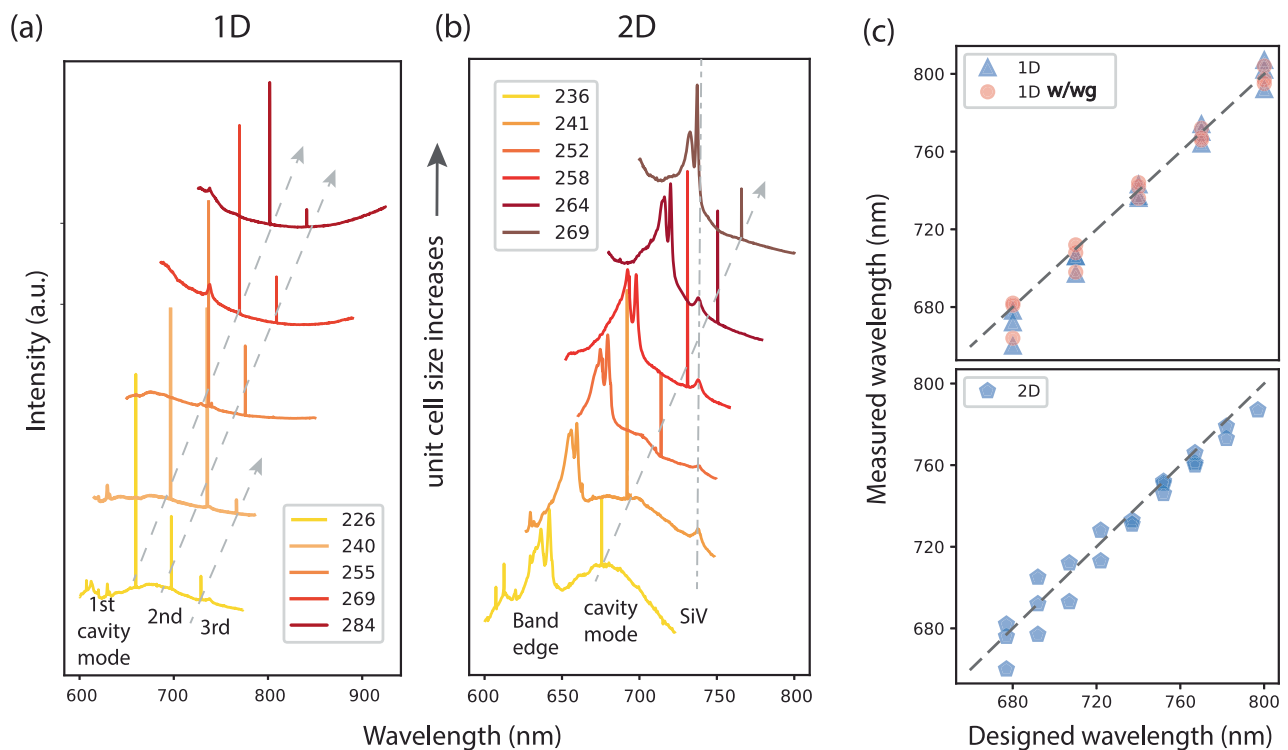


Fig. 3 | Lattice constant dependence of 1D and 2D PhC cavities. Off-resonance excitation and spectrometer characterization of (a) 1D and (b) 2D PhCs. The legend shows the unit cell length, in nm. The intensity is plotted against the wavelength, showing resonance features of the cavities and the SiV at 737 nm. The spectra are offset for clarity. The legend shows the corresponding design lattice constant a , in

nm. The cavity modes redshift as the lattice constant increases, as expected. c The measured cavity resonances (fundamental mode) versus the designed ones for 1D, 1D with taper, and 2D PhC cavities are presented in this paper. We observe excellent agreement between the two.

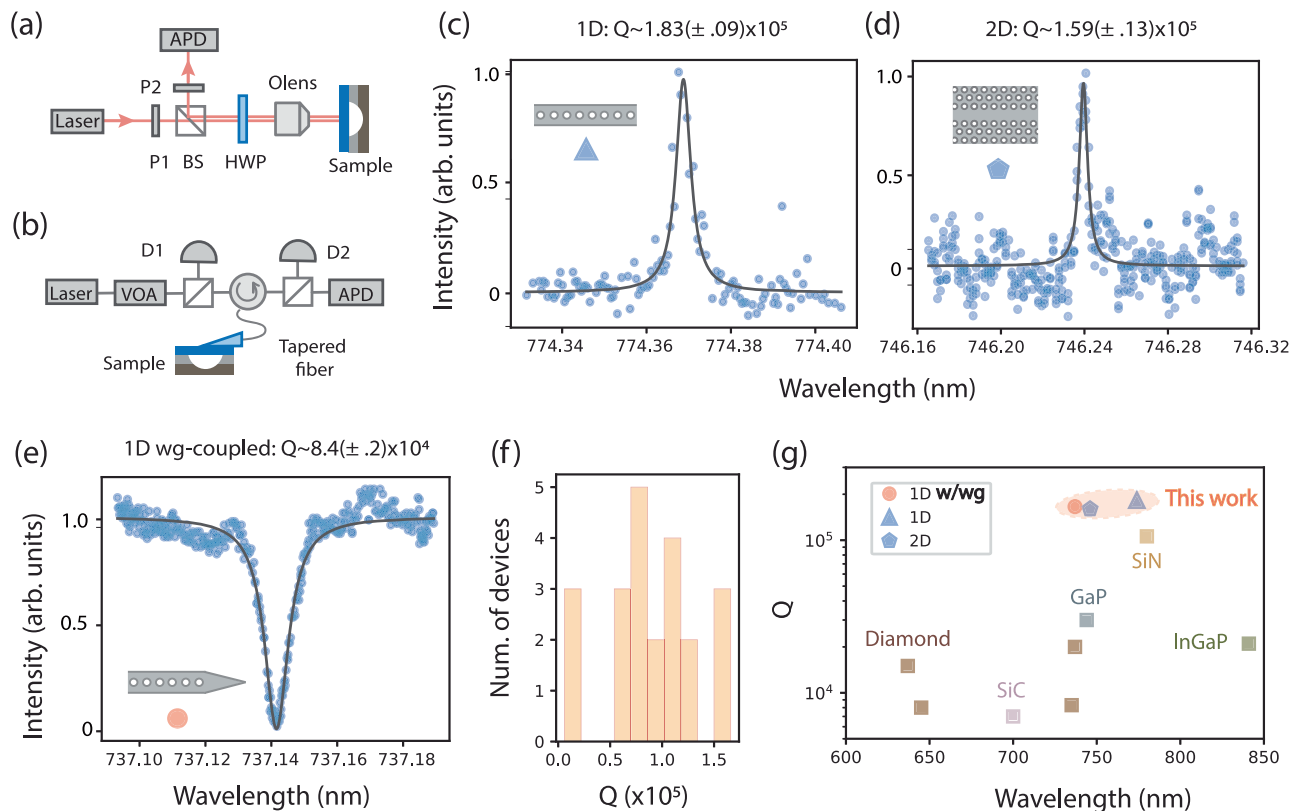


Fig. 4 | ID and 2D PhC cavity on-resonance characterizations for measuring quality factors. **a** The cross-polarization setup for on-resonance characterization of the cavity. Olens: objective lens; HWP: half-wave plate; BS: beam splitter; P1, P2: polarizers. **b** The fiber-coupling setup for on-resonance characterization of the cavity. VOA: variable optical attenuator; D1, D2: detectors. Laser: visible (710–790 nm) scanning laser; APD: avalanche photodiode. **c, d** On-resonance scan

of the 1D and 2D cavity using the cross-polarization setup. **e** On-resonance scan of the 1D cavity coupled to the feeding waveguide. The cavity is critically coupled as the contrast is ~95% in reflection. **f** Histogram of all the PhC cavities measured and resolved in the 710–770 nm range. **g** PhC cavity measurement summary. The values from this work are plotted along with the highest literature values in their respective categories, as shown in Table 1.

thermo-optic effect (see “Methods”). Figure 4e shows the cavity spectrum of the waveguide-coupled 1D PhC cavity with the highest Q factor. The loaded Q factor is measured to be 8.4×10^4 . The cavity dip shows full contrast ($95.3 \pm 0.3\%$ contrast), indicating that our cavity is almost critically coupled. This allows us to estimate the intrinsic Q to be $Q_i = (1.8 \pm 0.4) \times 10^5$. The coupling efficiency between the cavity and the waveguide is measured to be $\eta_c \sim 65\%$ in our system (see “Methods”).

Characterization of SiV properties

Stable and bright emitters are required for cavity quantum electrodynamics (QED) experiments. To demonstrate the immediate compatibility of this platform for an efficient photonic interface for emitters embedded in the diamond, we characterize the SiVs in the fabricated devices at 4 K and demonstrate optical coupling between a SiV and a high-Q 1D PhC cavity.

We optically characterize two single SiV centers embedded in the realized high-Q cavities by confocal PL measurements at 4 K, as shown in Fig. 5a. The spectrum of a SiV at 4 K features four optical transitions labeled from A to D around 737 nm, as shown in Fig. 5b. We first characterize the C transition of a single SiV at 737.09 nm. Figure 5d shows the color map of its photoluminescence excitation (PLE) spectra measured over two hours (upper panel) and a single scan spectrum (lower panel). There is no significant spectral diffusion, and the linewidth is fitted to be 605 MHz. The observed linewidth is slightly larger than the typical value of ion-implanted SiV⁻ centers³⁵, possibly due to the laser broadening and/or membrane/cavity fabrication³⁶. We then perform the second-order correlation ($g^{(2)}(\tau)$) measurements using a Hanbury Brown-Twiss setup (see “Methods”). The measured intensity

correlation histogram (Fig. 5c) exhibits a clear antibunching with a value of the zero time delay $g^{(2)}(0)$ of 0.31 ± 0.12 , confirming the single-photon nature of the investigated SiV. The non-zero value of $g^{(2)}(0)$ could be due to dark counts of the APD, drift of the sample position, and diffusion of the ZPL line over a long time.

We finally investigate the optical coupling between a single SiV center and a 1D cavity in our thin film diamond platform. We choose a cavity device with measured resonance at 737.5 nm and experimental Q of 1.2×10^5 . The measured PL spectra of the cavity device feature four sharp peaks, corresponding to A–D transitions of a SiV, and the cavity resonance, which is gradually tuned to the D line using a gas condensation approach¹² (Fig. 5e). The SiV experiences low strain, indicated by the ~55 GHz splitting between C and D line³⁷. We observe small shifts of the D line during the tuning, which could indicate changes in the strain environment. It is noted that the linewidth of the cavity spectra shown is limited by our spectrometer resolution of ~10 GHz. Under the resonance condition (spectral detuning between the D line and cavity of $\Delta \sim 0$ nm, red spectrum in Fig. 5e), we observe a ~20-fold intensity enhancement of the D line emission compared to that under far-detuned conditions ($\Delta \sim 0.4$ nm, blue spectrum in Fig. 5e) relative to the other lines, suggesting that the spontaneous emission rates of the SiV center are enhanced by Purcell effect.

We also conduct time-resolved PL measurements on the same SiV center (see “Method”). Figure 5f shows the PL curves measured under the resonance (red) and far-detuned condition (blue). By fitting the curves with a single exponential function with a constant offset, we obtain the lifetime of the SiV on resonance (τ_{on}) to be 0.47 ± 0.006 ns, which is reduced approximately by a factor of 3 from the off-resonance value (τ_{off}) of 1.3 ± 0.01 ns. The Purcell factor of the investigated zero-

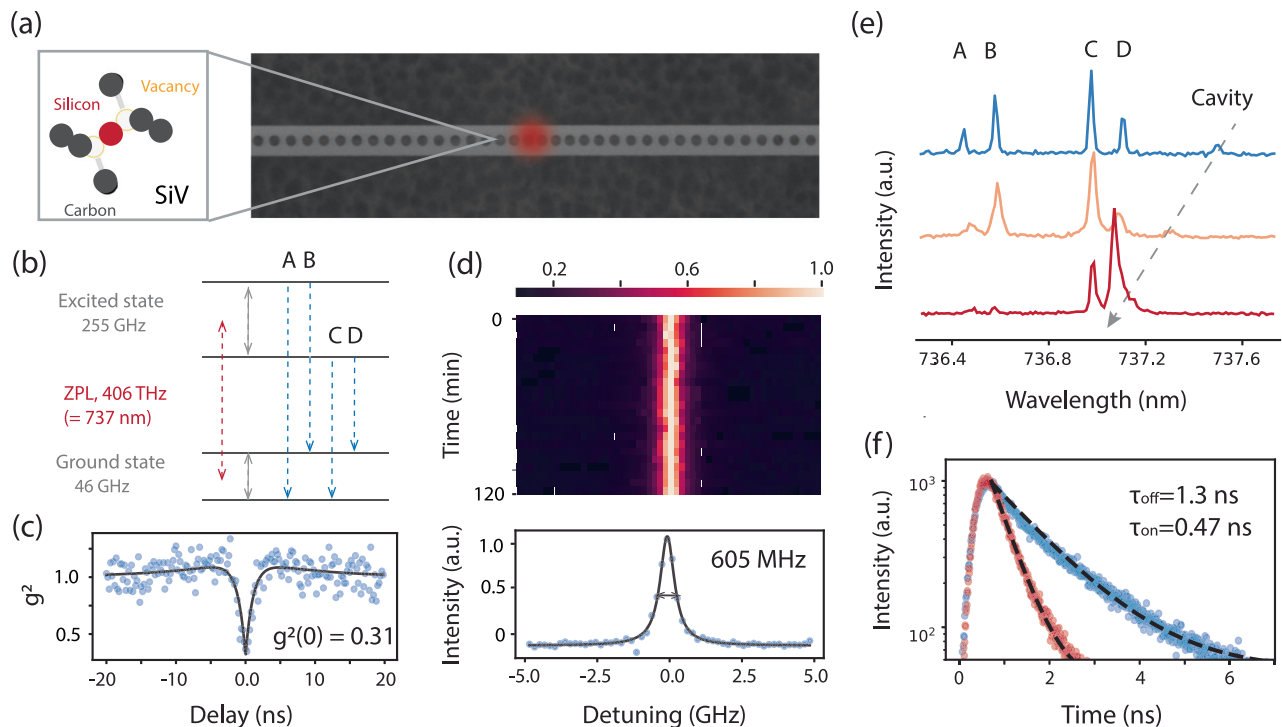


Fig. 5 | SiV characterization and its optical coupling to the PhC cavity at 4 K. **a** An illustration of SiV placed close to the center of PhC cavity (SEM image). SiV is an interstitial defect consisting of Si atoms positioned between two sites with missing carbon atoms in a diamond lattice. **b** A simplified level diagram of SiV, featuring A - D, 4 optical transitions around 737 nm. **c** Second-order autocorrelation measurement of the C line under on-resonant excitation. The $g^2(0) < 0.5$ confirms the single-photon nature of the emitter. **d** Top panel: the stability of the C line

of a SiV over two hours. The plot shows normalized intensity over time. The drift is much less than a linewidth; bottom panel: a scan of the C line at 120 min. **e** The photoluminescence (PL) spectra of the SiV as the cavity is tuned closer to the C and D lines. Each spectrum is normalized to the highest peak. The D line is getting much brighter as the cavity is tuned into resonance. **f** The measured lifetime of the SiV on and off-resonance (bulk) with the cavity, which shows a factor of 3 reductions. The two lifetimes correspond to the initial and final PL spectra in (e) of the same colors.

phonon line (ZPL) F_{ZPL} is estimated to be 13 (see “Methods”). This value is much smaller than the theoretical Purcell factor (see “Methods”), likely due to the large displacement of SiV position with respect to the cavity field maximum as a result of random bulk implantation. To further improve the Purcell factor, the SiVs can be implanted at the cavity region using the well-established masked implantation technique^{6,7}. We estimate that for SiV mask-implanted at the cavity regions, the cooperativity C , an important figure-of-merit for evaluating the emitter-cavity coupled system, could reach >960 (under-coupled, $Q \sim 1.8 \times 10^5$) or >440 (critically coupled, $Q \sim 8.4 \times 10^4$) with experimental values (see “Methods”), which are 9 or 4 times higher than the highest value reported in a previous work⁶. The realization of such a large C as a result of the high- Q cavity is highly advantageous for high fidelity of control of the spin/nuclear states and networking applications.

Discussion

We have demonstrated high- Q 1D and 2D PhC cavities using the thin film diamond approach. We achieved Q factors up to 1.8×10^5 , which is a record high in visible-wavelength PhC cavities in any materials. We also fabricated high- Q 2D PhC cavities that were previously challenging using conventional diamond bulk machining approaches and also achieved record-high Q values up to 1.6×10^5 . Finally, of interest for practical applications and demonstrations of efficient spin-photon interface, we demonstrated waveguide-coupled 1D PhC cavities featuring intrinsic (loaded) Q up to 1.8×10^5 (8.3×10^4) and coupling efficiency of 65%. The significant improvement of the experimental Q factors in this work can be attributed to the use of a high-optical-quality thin film diamond membrane with a smooth surface roughness < 0.3 nm and small thickness variation ~ 1 nm³². Still, Q s are one order of magnitude lower than theoretical predictions, indicating that there

is room for improvement. The difference could be due to surface absorption³⁸ and/or optical scatterings due to fabrication imperfections such as lithography error of the air holes in position or radius, surface roughness, sidewall roughness/tilt of air holes³⁹.

Lastly, we demonstrated optical coupling between the realized high Q cavity and a single SiV, with a measured Purcell factor of 13, and therefore the immediate compatibility of this platform with color-center cavity QED. Using masked implantation, better overlap between SiV and optical mode can be achieved, resulting in cooperativities >440 at ~ 100 mK (see “Method”). The lower loss and design flexibility in this platform can fundamentally enhance color-center-based technologies, by allowing for higher single photon rates, higher gate fidelities, more integrated functionalities, etc. In combination with the robust, high uniformity, and high-yield fabrication process, our thin-film diamond platform will hopefully unlock new opportunities for color-center applications for quantum information.

Our platform and fabrication approach based on a thin-film diamond can be applied to a variety of other micro/nanostructures that are important in diamond integrated photonic applications, such as nonlinear photonics^{40,41} and diamond phononics^{32,43}. In addition, the flexibility of direct bonding makes this approach easily applicable to other substrates besides Si/SiO₂³², which enables the heterogeneous integration of the diamond platform containing color centers onto existing and emerging integrated photonic circuits for quantum networks, including thin-film lithium niobate¹¹, aluminum nitride¹⁰, and CMOS-compatible platforms⁴⁴.

Methods

Confocal photoluminescence measurement setup

In Fig. 3, both spectra for 1D and 2D devices are measured using a commercial spectrometer system with free-space off-resonance

excitation and collection. A green diode laser (523 nm) is used to scatter off of the cavities via an objective ($\times 100$), and the scatter light is sent through a 1800 gr/mm grating and collected by a Si CCD camera cooled to 4 K. The spectrometer used is SpectraPro HRS-750, the supercontinuum laser is SuperK EXTREME.

Cross-polarized measurement setup

In Fig. 4, the visible scanning laser is M Squared, which can stabilize in 710–790 nm, and the APD is SPCM-AGRH-14-FC from Perkin Elmer. For these measurements, the input polarizer is aligned to the cavity polarization (TE), the half-wave plate is set to 23.5° so that the laser polarization is 45° relative to the cavity polarization, and the output polarization is set to be perpendicular to the cavity polarization. The working principle behind the measurement is that the cavity acts as a polarization filter when the incident light is resonant with the cavity. As such, off-resonant light is fully blocked by the cross-polarization between P1 and P2, but the light resonant with the cavity has a non-zero polarization component in the direction of P2, resulting in a Lorentzian peak in reflection corresponding to the cavity resonance.

Fiber-coupling measurement setup

The waveguide-coupled 1D PhC cavities are measured via fiber-coupled reflection measurements (shown in Fig. 4e). These measurements are performed by inputting light from a tunable laser (M Squared) into the diamond waveguide via a tapered optical fiber (S630 HP)³³ and measuring the reflected light from the optical cavity.

Data availability

The data supporting this study's findings are available from the corresponding author (S.W.D.) upon request.

References

1. Miller, B. S. et al. Spin-enhanced nanodiamond biosensing for ultrasensitive diagnostics. *Nature* **587**, 588–593 (2020).
2. Mamin, H. J. et al. Nanoscale nuclear magnetic resonance with a nitrogen-vacancy spin sensor. *Science* **339**, 557–560 (2013).
3. Zhao, N. et al. Sensing single remote nuclear spins. *Nat. Nanotechnol.* **7**, 657–662 (2012).
4. Glenn, D. R. et al. High-resolution magnetic resonance spectroscopy using a solid-state spin sensor. *Nature* **555**, 351–354 (2018).
5. Hermans, S. L. N. et al. Qubit teleportation between non-neighbouring nodes in a quantum network. *Nature* **605**, 663–668 (2022).
6. Bhaskar, M. K. et al. Experimental demonstration of memory-enhanced quantum communication. *Nature* **580**, 60–64 (2020).
7. Stas, P.-J. et al. Robust multi-qubit quantum network node with integrated error detection. *Science* **378**, 557–560 (2022).
8. Parker, R. A. et al. A diamond nanophotonic interface with an optically accessible deterministic electronuclear spin register. *Nat. Photonics* **18**, 1–6 (2023).
9. Zhang, J. L. et al. Strongly cavity-enhanced spontaneous emission from silicon-vacancy centers in diamond. *Nano Lett.* **18**, 1360–1365 (2018).
10. Maity, S. et al. Coherent acoustic control of a single silicon vacancy spin in diamond. *Nat. Commun.* **11**, 193 (2020).
11. Riedel, D. et al. Efficient photonic integration of diamond color centers and thin-film lithium niobate. *ACS Photonics* **10**, 4236–4243 (2023).
12. K. Kuruma. et al. Coupling of a single tin-vacancy center to a photonic crystal cavity in diamond. *Appl. Phys. Lett.* **118**, 230601 (2021).
13. Rugar, A. E. et al. Quantum photonic interface for tin-vacancy centers in diamond. *Phys. Rev. X* **11**, 031021 (2021).
14. Guo, X. et al. Microwave-based quantum control and coherence protection of tin-vacancy spin qubits in a strain-tuned diamond-membrane heterostructure. *Phys. Rev. X* **13**, 041037 (2023).
15. Ruf, M., Weaver, M. J., van Dam, S. B. & Hanson, R. Resonant excitation and Purcell enhancement of coherent nitrogen-vacancy centers coupled to a Fabry-perot microcavity. *Phys. Rev. Appl.* **15**, 024049 (2021).
16. Khanaliloo, B., Mitchell, M., Hryciw, A. C. & Barclay, P. E. High-Q/V monolithic diamond microdisks fabricated with quasi-isotropic etching. *Nano Lett.* **15**, 5131–5136 (2015).
17. Khanaliloo, B. et al. Single-crystal diamond nanobeam waveguide optomechanics. *Phys. Rev. X* **5**, 041051 (2015).
18. Mouradian, S., Wan, N. H., Schröder, T. & Englund, D. Rectangular photonic crystal nanobeam cavities in bulk diamond. *Appl. Phys. Lett.* **111**, 021103 (2017).
19. Jung, T. et al. Spin measurements of NV centers coupled to a photonic crystal cavity. *APL Photonics* **4**, 120803 (2019).
20. Sun, S., Kim, H., Luo, Z., Solomon, G. S. & Waks, E. A single-photon switch and transistor enabled by a solid-state quantum memory. *Science* **361**, 57–60 (2018).
21. Saggio, V., et al. Cavity-enhanced single artificial atoms in silicon. *Nat Commun* **15**, 5296 (2024).
22. Lukin, D. M. et al. 4H-silicon-carbide-on-insulator for integrated quantum and nonlinear photonics. *Nat. Photonics* **14**, 330–334 (2019).
23. Crook, A. L. et al. Purcell enhancement of a single silicon carbide color center with coherent spin control. *Nano Lett.* **20**, 3427–3434 (2020).
24. Yang, L., Wang, S., Shen, M., Xie, J. & Tang, H. X. Controlling single rare earth ion emission in an electro-optical nanocavity. *Nat. Commun.* **14**, 1718 (2023).
25. Zhong, T., Kindem, J. M., Miyazono, E. & Faraon, A. Nanophotonic coherent light-matter interfaces based on rare-earth-doped crystals. *Nat. Commun.* **6**, 8206 (2015).
26. Raha, M. et al. Optical quantum nondemolition measurement of a single rare earth ion qubit. *Nat. Commun.* **11**, 1605 (2020).
27. Burek, M. J. et al. High quality-factor optical nanocavities in bulk single-crystal diamond. *Nat. Commun.* **5**, 5718 (2014).
28. Chia, C. Quantum optomechanics with color centers in diamond. (Harvard University, (2021).
29. Kuruma, K. et al. Telecommunication-wavelength two-dimensional photonic crystal cavities in a thin single-crystal diamond membrane. *Appl. Phys. Lett.* **119**, 171106 (2021).
30. Jung, T. et al. Reproducible fabrication and characterization of diamond membranes for photonic crystal cavities. *Phys. Status Solidi* **213**, 3254–3264 (2016).
31. Lee, J. C. et al. Deterministic coupling of delta-doped nitrogen vacancy centers to a nanobeam photonic crystal cavity. *Appl. Phys. Lett.* **105**, 261101 (2014).
32. Guo, X. et al. Direct-bonded diamond membranes for heterogeneous quantum and electronic technologies. Preprint at arXiv <https://doi.org/10.48550/arXiv.2306.04408> (2023).
33. Burek, M. J. et al. Fiber-coupled diamond quantum nanophotonic interface. *Phys. Rev. Appl.* **8**, 024026 (2017).
34. Zeng, B. et al. Cryogenic packaging of nanophotonic devices with a low coupling loss <1 dB. *Appl. Phys. Lett.* **123**, 161106 (2023).
35. Evans, R. E., Sipahigil, A., Sukachev, D. D., Zibrov, A. S. & Lukin, M. D. Narrow-linewidth homogeneous optical emitters in diamond nanostructures via silicon ion implantation. *Phys. Rev. Appl.* **5**, 044010 (2016).
36. Guo, X. et al. Tunable and transferable diamond membranes for integrated quantum technologies. *Nano Lett.* **21**, 10392–10399 (2021).
37. Meesala, S. et al. Strain engineering of the silicon-vacancy center in diamond. *Phys. Rev. B Condens. Matter* **97**, 205444 (2018).
38. Asano, T., Ochi, Y., Takahashi, Y., Kishimoto, K. & Noda, S. Photonic crystal nanocavity with a Q factor exceeding eleven million. *Opt. Express* **25**, 1769–1777 (2017).

39. Asano, T., Song, B.-S. & Noda, S. Analysis of the experimental Q factors (~1 million) of photonic crystal nanocavities. *Opt. Express* **14**, 1996–2002 (2006).
40. Hausmann, B. J. M., Bulu, I., Venkataraman, V., Deotare, P. & Lončar, M. Diamond nonlinear photonics. *Nat. Photonics* **8**, 369–374 (2014).
41. Latawiec, P. et al. On-chip diamond Raman laser. *Optica* **2**, 924 (2015).
42. Burek, M. J. et al. Diamond optomechanical crystals. *Optica* **3**, 1404–1411 (2016).
43. Overtchayapong, P., Lee, K. W., Myers, B. A. & Jayich, A. C. B. Dynamic strain-mediated coupling of a single diamond spin to a mechanical resonator. *Nat. Commun.* **5**, 4429 (2014).
44. Kim, D. et al. A CMOS-integrated quantum sensor based on nitrogen–vacancy centres. *Nat. Electron.* **2**, 284–289 (2019).
45. Samutpraphoot, P. et al. Strong coupling of two individually controlled atoms via a nanophotonic cavity. *Phys. Rev. Lett.* **124**, 063602 (2020).
46. Sergent, S. et al. High-Q AlN ladder-structure photonic crystal nanocavity fabricated by layer transfer. *Phys. Status Solidi C* **10**, 1517–1520 (2013).
47. Bracher, D. O. & Hu, E. L. Fabrication of High-Q nanobeam photonic crystals in epitaxially grown 4H-SiC. *Nano Lett.* **15**, 6202–6207 (2015).
48. Chakravarthi, S. et al. Hybrid integration of GaP photonic crystal cavities with silicon-vacancy centers in diamond by stamp-transfer. *Nano Lett.* **23**, 3708–3715 (2023).
49. Saber, I. et al. Photonic crystal nanobeam cavities with optical resonances around 800 nm. *JOSA B* **36**, 1823–1828 (2019).

Acknowledgements

The authors thank Dr. C. De-Eknamkul, Dr. B. Pingault, and Dr. R. Katsumi for their helpful discussions. Research reported in this publication was supported as part of the AWS Center for Quantum Networking’s research alliance with the Harvard Quantum Initiative (or HQI), NSF ERC (EEC-1941583), ONR (N00014-20-1-2425), AFOSR (FA9550-20-1-0105 and MURI on Quantum Phononics), ARO MURI (W911NF1810432). The membrane synthesis is funded through Q-NEXT, supported by the U.S. Department of Energy, Office of Science, and National Quantum Information Science Research Centers. The membrane bonding work is supported by NSF award AM-2240399 and made use of the Pritzker Nanofabrication Facility (Soft and Hybrid Nanotechnology Experimental Resource, NSF ECCS-2025633) and the Materials Research Science and Engineering Center (NSF DMR-2011854) at the University of Chicago. Diamond growth-related efforts were supported by the U.S. Department of Energy, Office of Basic Energy Sciences, Materials Science and Engineering Division (N.D.).

Author contributions

S.W.D., K.K., and M.L. conceived the experiment; S.W.D. fabricated the devices; M.H., S.W.D., and C.J. performed cavity and SiV measurements; S.W.D and M.H. performed data analysis. X.G. and Z.L. prepared the thin-film sample; K.K. performed the FDTD simulation; N.D. performed the diamond synthesis; S.W.D wrote the manuscript with input from all co-authors. M.L., A.H., D.D.A., and F.J.H. participated in and supervised the project.

Competing interests

The authors declare no competing interests.

Additional information

Supplementary information The online version contains supplementary material available at <https://doi.org/10.1038/s41467-024-50667-5>.

Correspondence and requests for materials should be addressed to Sophie W. Ding, Alexander A. High or Marko Loncar.

Peer review information *Nature Communications* thanks the anonymous, reviewers for their contribution to the peer review of this work. A peer review file is available.

Reprints and permissions information is available at <http://www.nature.com/reprints>

Publisher’s note Springer Nature remains neutral with regard to jurisdictional claims in published maps and institutional affiliations.

Open Access This article is licensed under a Creative Commons Attribution-NonCommercial-NoDerivatives 4.0 International License, which permits any non-commercial use, sharing, distribution and reproduction in any medium or format, as long as you give appropriate credit to the original author(s) and the source, provide a link to the Creative Commons licence, and indicate if you modified the licensed material. You do not have permission under this licence to share adapted material derived from this article or parts of it. The images or other third party material in this article are included in the article’s Creative Commons licence, unless indicated otherwise in a credit line to the material. If material is not included in the article’s Creative Commons licence and your intended use is not permitted by statutory regulation or exceeds the permitted use, you will need to obtain permission directly from the copyright holder. To view a copy of this licence, visit <http://creativecommons.org/licenses/by-nc-nd/4.0/>.

© The Author(s) 2024